ACS APPLIED MATERIALS & INTERFACES

www.acsami.org

Research Article

Gate-Modulated Ultrasensitive Visible and Near-Infrared Photodetection of Oxygen Plasma-Treated WSe_2 Lateral pn-Homojunctions

Sekhar Babu Mitta, Fida Ali, Zheng Yang, Inyong Moon, Faisal Ahmed, Tae Jin Yoo, Byoung Hun Lee, and Won Jong Yoo*

Cite This: *ACS Appl. Mater. Interfaces* 2020, 12, 23261−23271

Read Online

ACCESS | Metrics & More | Article Recommendations | Supporting Information

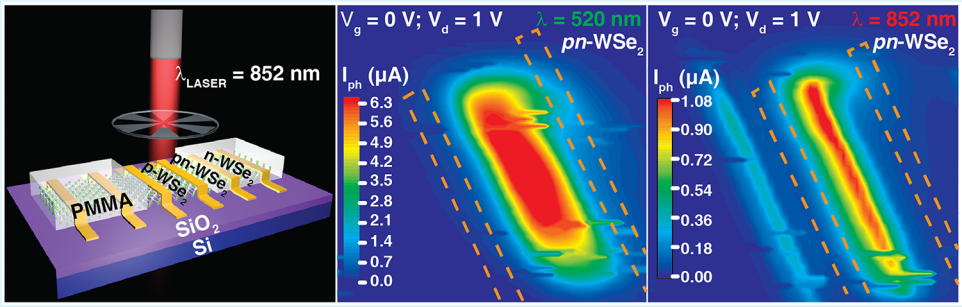

ABSTRACT: We investigate the development of gate-modulated tungsten diselenide (WSe_2)-based lateral pn-homojunctions for visible and near-infrared photodetector applications via an effective oxygen (O_2) plasma treatment. O_2 plasma acts to induce the p-type WSe_2 for the otherwise n-type WSe_2 by forming a tungsten oxide (WO_x) layer upon O_2 plasma treatment. The WSe_2 lateral pn-homojunctions displayed an enhanced photoresponse and resulted in open-circuit voltage (V_{OC}) and short-circuit current (I_{SC}) originating from the pn-junction formed after O_2 plasma treatment. We further notice that the amplitude of the photocurrent can be modulated by different gate biases. The fabricated WSe_2 pn-homojunctions exhibit greater photoresponse with photoresponsivities (ratio of the photocurrent and incident laser power) of 250 and 2000 mA/W, high external quantum efficiency values (%, total number of charge carriers generated for the number of incident photons on photodetectors) of 97 and 420%, and superior detectivity values (magnitude of detector sensitivity) of 7.7×10^9 and 7.2×10^{10} Jones upon illumination with visible (520 nm) and near-infrared lasers (852 nm), respectively, at low bias (V_g = 0 V and V_d = 1 V) at room temperature, demonstrating very high-performance in the IR region superior to the contending two-dimensional material-based photonic devices. These superior optoelectronic properties are attributed to the junctions induced by O_2 plasma doping, which facilitate the effective carrier generation and separation of photocarriers with applied external drain bias upon strong light absorption.

KEYWORDS: *gate modulation, infrared photodetection, WSe_2, O_2 plasma doping, lateral pn-homojunctions*

INTRODUCTION

The two-dimensional (2D) transition-metal dichalcogenides (TMDCs) with a layered semiconducting structure offer a unique platform to investigate and develop future nanoscale devices. Indeed, TMDCs are utilized in optoelectronic applications such as photodetectors, solar cells, light-emitting diodes, and photovoltaic cells owing to their tunable band gap controlled by the number of layers.[1−3] The pn-junctions are the functional building blocks of various optoelectronic devices; on the other hand, bulk semiconductor-based pn-junctions employed in modern optoelectronic devices hold certain limitations such as high cost, mechanical rigidity, and bandwidth coverage. In recent years, with the advent of atomically thin van der Waals (vdW) structures, 2D material-based pn-junction photodetectors have been demonstrated with tremendous efforts owing to their atomic thinness, mechanical flexibility, and large-scale development,[4−6] whereas the electrically driven light emission in graphene-based pn-junction photodetectors is challenging and did not show diode-like rectification behavior due to its zero band gap. Recently, the vdW vertical pn-heterojunctions are developed as a novel section of artificial structures; however, to accomplish this, complex processing such as an accurate alignment and

Received: December 28, 2019
Accepted: April 29, 2020
Published: April 29, 2020

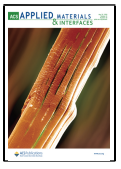

https://dx.doi.org/10.1021/acsami.9b23450
ACS Appl. Mater. Interfaces 2020, 12, 23261−23271

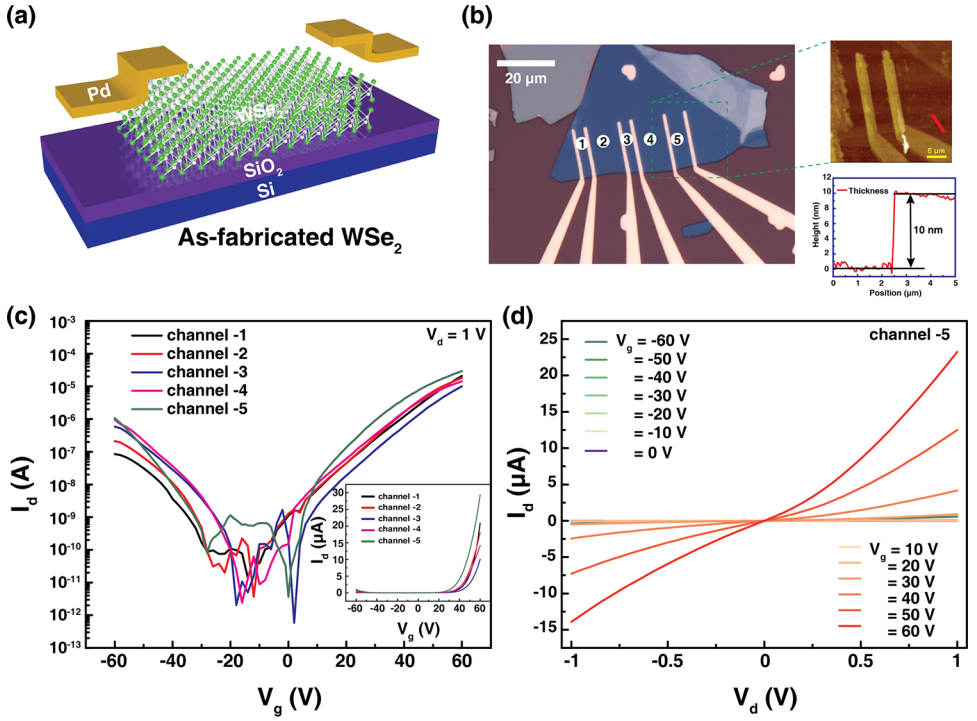

Figure 1. Characterization of multilayered WSe_2 on the Si/SiO_2 substrate. (a) Schematic representation of as-fabricated bulk WSe_2 FET fabricated on the Si/SiO_2 substrate. (b) Optical microscopy (OM) image of the as-fabricated WSe_2 FET with Pd contacts indicating five different channels (1−5). The zoomed part on top right shows an AFM image of a WSe_2 flake, and the bottom-right part displays the AFM height profile revealing the thickness of the ∼10 nm WSe_2 flake. (c) Transfer characteristics of as-fabricated WSe_2 FET obtained for all the five channels measured at V_d = 1 V in logarithmic scale and the inset displaying the transfer curves in linear scale. (d) Output curves of WSe_2 FET measured at V_g sweep of −60 to +60 V with 10 V step.

multitransfer technology is required and is hard to localize on a flake during the device fabrication process, in which the vdW gaps at the junctions can inhibit the charge transfer and deteriorate the device performance. Cheng et al. demonstrated atomically thin vertical WSe_2/MoS_2 pn-heterojunction diodes, which resulted in a low quantum efficiency of 12%.[7] In addition, the pn-junctions are achieved via chemical doping or electrical tuning in which the impurities are introduced at the interface or require an external electric field.[5−11]

Among the various 2D TMDCs, tungsten diselenide (WSe_2) with a bulk indirect band gap of ∼1.2 eV exhibits an ambipolar behavior when utilized as a channel material for field-effect transistors (FETs), while it can be an ideal material for optoelectronic applications due to its tunable energy bands, fast charge transfer, and strong optical absorption.[12−15] To enrich the TMDC optoelectronic device performances, utilization of the appropriate charge doping process becomes noteworthy with either being hole-rich or electron-rich. Recently, the functionalization of WSe_2 has received significant attention as a highly efficient technique to enhance the device performance via electrostatic or chemical doping to achieve pn-junction photodetectors; however, the devices accomplished by electrostatic gating involve complex design as well as the stress induced by gating limit the optoelectrical performance and stability of pn-junctions.[4,16−18] For example, Baugher et al. reported the electrically tunable pn-junction photodetectors by the electrostatic gating of WSe_2 flake, and these photodetectors demonstrated a photoresponsivity of 210 mA/W and external quantum efficiency of 0.2%.[16] Also, Xie et al. demonstrated a WSe_2 lateral pn-junction with a high rectifying ratio of 10^6 and photoresponsivity of 2.49 A/W by selective N_2O plasma exposure.[17] Addou et al. also recently reported that the oxidation of chemical vapor deposition-grown WSe_2 can be induced by exposure to air.[19] These various choices of doping techniques are yielding exciting opportunities to WSe_2 as a promising material for future optoelectronic devices by rendering high absorption efficiency and responsivity. Among the doping methodologies, O_2 plasma treatment is a semiconductor industry-compatible process, which can be easily adapted for doping in the semiconductor manufacturing process.[20−23] In addition, the surface treatment on TMDCs by using O_2 plasma is investigated for the enhancement of the electrical performances. The monolayered WSe_2 p-FETs with chemically degenerated doped contacts and with surface treatment exhibit a high hole mobility of 250 $cm^2/V{\cdot}s$ and maximum hole concentration of $\sim 10^{19}/cm^3$.[24,25]

Infrared (IR) photodetectors have been used extensively in diverse applications such as telecommunications, bio-imaging, thermal imaging, military, night vision, etc. Moreover, the 2D TMDC materials interact with a wide range of spectra from ultraviolet (UV) to terahertz frequencies and have attracted great research interest in the field of IR photodetection to demonstrate exceptional optoelectrical properties.[26−31] Nevertheless, the WSe_2-based photodetectors are restricted to IR light detection and have not been widely demonstrated due to the direct band gap of 1.6 eV for monolayer WSe_2, and also, reports on bulk WSe_2 typically focus on visible region detection.[15,17] To circumvent this, here, we demonstrate simple and effective fabrication of O_2 plasma-doped multilayer WSe_2 lateral pn-homojunctions employed for broadband (visible and near-infrared) photodetector application with different gate voltage tuning. The typical transfer curves exhibit

https://dx.doi.org/10.1021/acsami.9b23450
ACS Appl. Mater. Interfaces 2020, 12, 23261−23271

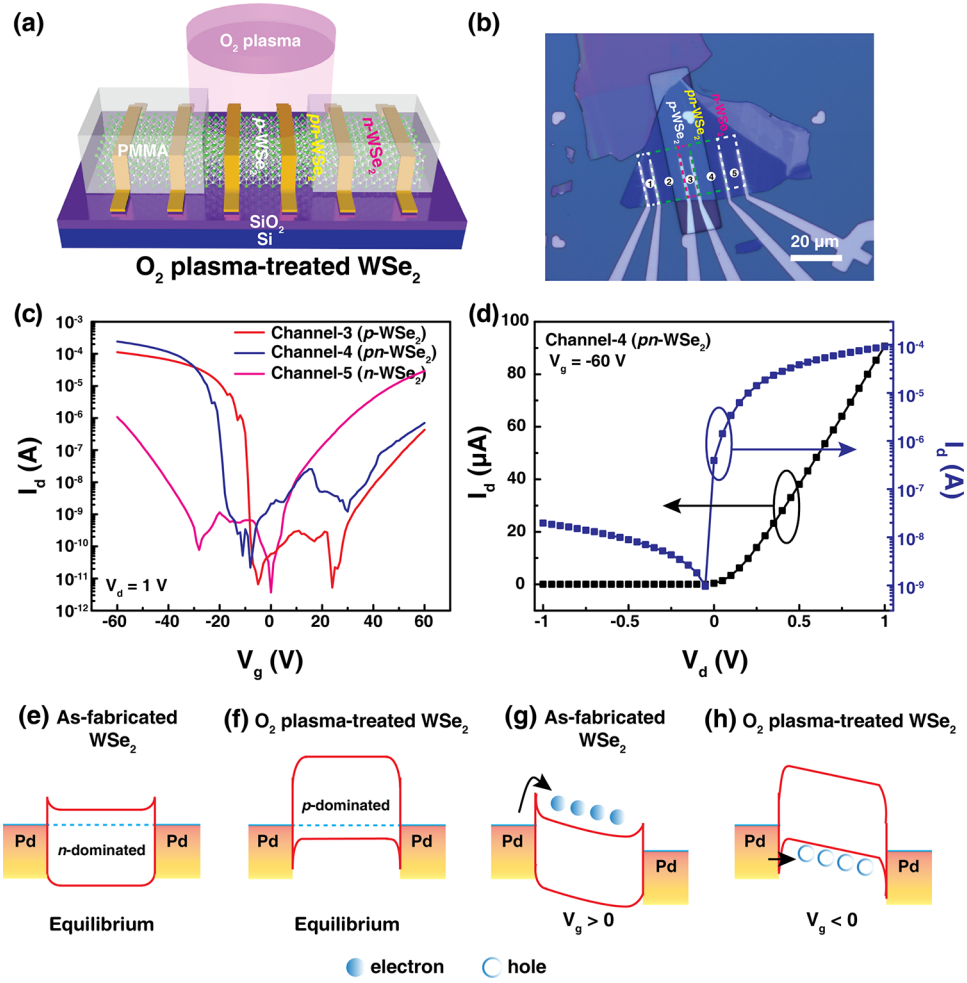

Figure 2. Characterization of the WSe_2 FET device after oxygen (O_2) plasma treatment. (a) Schematic illustration of O_2 plasma treatment to bulk WSe_2 FET with the opened and PMMA-covered regions. (b) OM image of O_2 plasma-treated WSe_2 FET device showing channels 3, 4, and 5 as p-WSe_2, pn-WSe_2, and n-WSe_2, respectively. (c) Transfer curves of p-, pn-, and n-WSe_2 channels measured at V_d = 1 V after O_2 plasma treatment are represented in logarithmic scale. (d) The output curve of O_2 plasma-treated WSe_2 FET (pn-WSe_2) obtained at V_g = −60 V is represented in both linear and logarithmic scales. (e−h) The corresponding energy band diagrams depict the carrier transport paths in WSe_2 before and after O_2 plasma treatment at applied gate bias.

the n-type and p-type behaviors of WSe_2 before and after O_2 plasma treatment, respectively, which are attributed to the fact that O_2 plasma acts as a p-type dopant by forming a tungsten oxide (WO_x) layer. We analyzed the Raman spectroscopy and photoluminescence (PL); nevertheless, the formation of the tungsten oxide (WO_x) layer is scrutinized using X-ray photoelectron spectroscopy (XPS). The WSe_2 lateral pn-homojunctions exhibit unique properties like short-circuit current (I_{SC}) and open-circuit voltage (V_{OC}) with an enhanced photoresponse generated from the pn-junction formed after O_2 plasma treatment. The device displays a novel feature in the transfer characteristics under gate modulation and reveals efficient near-IR photodetecting properties. Upon visible (520 nm) and near-IR laser illuminations (852 nm), the photodetection properties of pn-WSe_2 homojunctions such as photoresponsivities, EQE, response time, and detectivity are greatly enhanced compared to those of as-fabricated WSe_2. The scanning photomapping spectroscopy of pn-WSe_2 also demonstrates the origin of photocurrent generation from the junctions. This promising 2D homojunction induced by the O_2 plasma doping process will facilitate the development of broadband photodetectors and future electronics applications.

RESULTS AND DISCUSSION

Figure 1a illustrates the schematic of a WSe_2 device fabricated on a Si/SiO_2 substrate. The whole process of exfoliation and fabrication was performed inside the glove box with a controlled inert environment. The fabrication process is described in Materials and Methods. An optical microscopy (OM) image of the as-fabricated WSe_2 FET device (with channels 1−5) is shown in Figure 1b. The top right side of Figure 1b shows the AFM image of WSe_2 channel 5 acquired from the dashed square area, and the bottom right side shows the AFM height profile, which reveals the thickness of the ∼10 nm WSe_2 flake. Initially, the electrical characteristics of as-fabricated WSe_2 FET were investigated under vacuum conditions (∼5 mTorr pressure) at room temperature. The transfer characteristics of all the WSe_2 channels (1−5) obtained at V_d = +1 V exemplify an ambipolar behavior with a higher current level at V_g > 0, as shown in Figure 1c. An n-dominant ambipolar trend unveiled that the electron current (at V_g = +60 V) was more than 2 orders of magnitude higher than the hole current (at V_g = −60 V) and showed that the Fermi level lies near to the conduction band of WSe_2. This might be due to the specific band alignment between Pd and

https://dx.doi.org/10.1021/acsami.9b23450
ACS Appl. Mater. Interfaces 2020, 12, 23261−23271

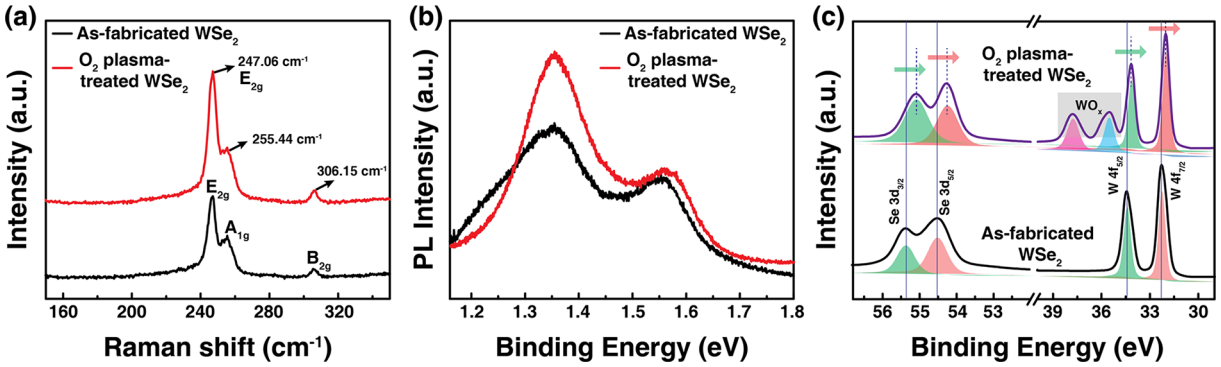

Figure 3. (a) Raman, (b) photoluminescence (PL), and (c) X-ray photoelectron spectroscopy (XPS) spectra of the WSe_2 device measured before and after O_2 plasma treatment. The Raman spectra reveal that no change is observed in Raman peaks with O_2 plasma treatment. From the PL analysis, the PL intensities at 1.35 and 1.55 eV were enhanced after O_2 plasma doping. The XPS spectra comparison of as-fabricated and O_2 plasma-treated WSe_2 flakes clearly shows the existence of two extra peaks at the binding energies of 35.53 and 37.68 eV corresponding to WO_x and shift in binding energies (dashed lines) of W and Se peaks after O_2 plasma treatment. The shifts in binding energy are shown with green and red arrows for both W and Se peaks after O_2 plasma treatment.

WSe_2, unintentional n-doping by Se vacancies in WSe_2, and/or impurities.[32] Besides, the output curves of the as-fabricated WSe_2 FET measured at various gate voltages (V_g = −60 to +60 V) are displayed in Figure 1d. Here, we observed a nonlinear trend from the output characteristics at all the applied gating conditions, which suggested the formation of Schottky contacts between metal electrodes (Pd) and the WSe_2 channel.

As observed from the as-fabricated WSe_2 FET characteristics, the electron current is dominated under high positive gate bias, and therefore, to achieve the hole-dominated current, it is essential to modulate the as-fabricated WSe_2 channels with O_2 plasma, which acts as a p-type dopant upon exposure to the controlled plasma conditions.[17,24,25] Figure 2 demonstrates the electrical performances of O_2 plasma-treated WSe_2 FET devices. The as-fabricated WSe_2 devices were covered with polymethylmethacrylate (PMMA), and a rectangular window was opened on a channel by employing electron-beam lithography (EBL) followed by O_2 plasma treatment. The O_2 plasma, generated with the optimized plasma operating conditions (see device fabrication), were exposed to the WSe_2 FET device, as illustrated in Figure 2a. The O_2 molecules were chemisorbed on top of the WSe_2 surface, and consequently, the Se atoms were replaced by O atoms, which resulted in the formation of a WO_x layer on top of the WSe_2 flake. Figure 2b depicts an OM image of the O_2 plasma-treated WSe_2 FET device. The thickness of WO_x generated after O_2 plasma treatment is found to be approximately ∼1 nm, which can be analyzed by employing time-of-flight secondary ion mass spectroscopy measurements.[23] Here, channel 3 (to achieve p-type WSe_2) and channels 2 and 4 (to achieve WSe_2 pn-homojunction) were completely and partially opened with PMMA, respectively, whereas channels 1 and 5 (n-WSe_2) were covered with PMMA. The WSe_2 pn-homojunction used in this study consists of the n-side coated with PMMA. Initially, we carried out the electronic transport and time-resolved photocurrent measurements on the as-fabricated WSe_2, comparing the results without and with PMMA to investigate the possible dielectric screening effects induced by PMMA, as illustrated in Figure S2 (Supporting Information). Here, we did not observe noticeable difference in the electronic transport and interpreted that these unchanged electrical properties were due to short-range scattering, which dominated over long-range scattering. In addition, the photocurrent from the WSe_2 pn-homojunction should be independent of the dielectric screening, different from usual electronic carrier transport. Therefore, we understood that the photocurrent obtained with bottom SiO_2 and top n-side coated with PMMA in this study represents accurate photonic performance.

The effect of O_2 plasma doping (p-type doping) on as-fabricated WSe_2 FET devices was confirmed through the electrical characteristics. The typical transfer curves of three different channels, i.e., channels 3 (p-WSe_2), 4 (pn-WSe_2), and 5 (n-Wse_2), are compiled in Figure 2c, in which channel 3 and the half-portion of channel 4 resulted in yielding of p-type characteristics from n-type. The output curve of channel 4 (pn-WSe_2) signifying the forward rectifying diode behavior is shown in Figure 2d, which implied that the drain current (I_d) under forward bias (V_d > 0 V) is much higher than the I_d under reverse bias (V_d < 0 V). The transfer characteristics of as-fabricated and O_2 plasma-doped WSe_2 FET for five different channels (1−5) and the output curves of pn-WSe_2 FET measured with respect to V_g sweep are displayed in Figure S3 (Supporting Information). The corresponding energy band diagrams depicting the carrier transport paths in WSe_2 at applied gate bias are illustrated in Figure 2e−h. The band alignments of Pd and WSe_2 for n-dominated (n-WSe_2) and p-dominated (p-WSe_2) WSe_2 in the equilibrium state are illustrated in Figure 2e,f, respectively. At large positive V_g (V_g > 0 V), more electrons accumulated in the conduction band, leading to the increase in electron current level (Figure 2g). In contrast, owing to the p-doping effect of O_2 plasma (formation of a WO_x layer on top of WSe_2) and the application of large negative V_g (V_g < 0 V), the Schottky barrier width along the Pd/WSe_2 interface was thinned, aiding the injection of hole carriers into the WSe_2 channel across the barrier and thereby resulting in a large hole current, as shown in Figure 2h.

Further characterizations of WSe_2 flakes were carried out by Raman spectroscopy and photoluminescence (PL). Figure 3a displays the characteristic Raman spectra of the WSe_2 flake with peak position values acquired before and after O_2 plasma treatment. We observed the typical Raman peaks of WSe_2 at 247.06 and 255.44 cm^{-1}, which represent in-plane vibrational E_{2g} mode and out-of-plane vibrational A_{1g} mode, respectively, and the bulk B_{2g} mode (observed in multilayer and bulk) at 306.56 cm^{-1}. We did not observe any characteristic Raman peak shift upon O_2 plasma treatment compared to the pristine

https://dx.doi.org/10.1021/acsami.9b23450
ACS Appl. Mater. Interfaces 2020, 12, 23261−23271

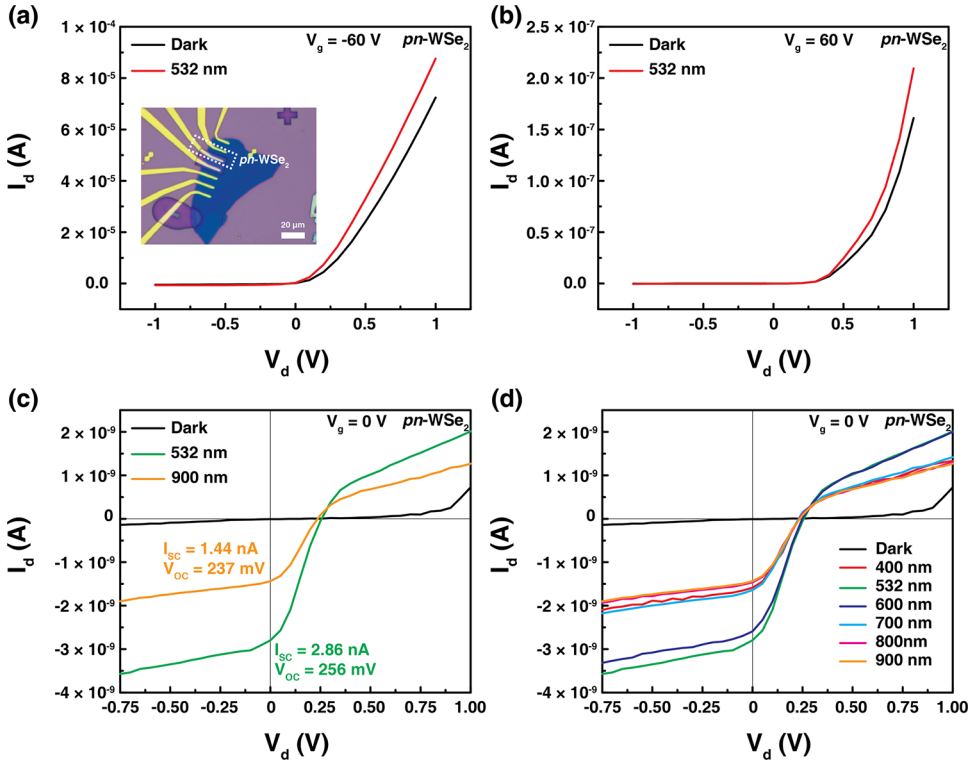

Figure 4. Photoresponse characteristics of pn-WSe_2 homojunction FET devices. (a, b) I_d–V_d characteristics of pn-WSe_2 measured in the dark and under 532 nm light illumination obtained at V_g = −60 and +60 V, respectively. The inset in (a) shows the OM image of the device and the measured pn-WSe_2 is represented in a white dotted box. (c) I_d–V_d characteristics of pn-WSe_2 measured in the dark and under 532 and 900 nm light illuminations demonstrating photovoltaic behavior at V_d = V_g = 0 V, which exhibits a short-circuit current (I_{SC}) and open-circuit voltage (V_{OC}). (d) I_d–V_d characteristics of pn-WSe_2 measured in the dark and under various light illuminations.

WSe_2 flake, similar to that reported earlier.[33] Subsequently, as shown in Figure 3b, the bulk WSe_2 device exhibited two main PL peaks at 1.35 and 1.55 eV before O_2 plasma treatment; however, the intensities of PL peaks were enhanced after O_2 plasma doping. To further verify the formation of the WO_x layer on top of WSe_2 after O_2 plasma treatment, we performed XPS for WSe_2 before and after O_2 plasma treatment, as shown in Figure 3c. The XPS core spectrum of WSe_2 showed two significant peaks of W (Se) at 32.28 eV (54.53 eV) and 34.43 eV (55.38 eV) corresponding to W $4f_{7/2}$ (Se $3d_{5/2}$) and W $4f_{5/2}$ (Se $3d_{3/2}$), respectively.[25] After O_2 plasma treatment, two additional peaks at the binding energies of 35.53 and 37.68 eV appeared in the XPS core spectrum corresponding to WO_x ($x \leq 3$).[33−35] Moreover, the shifts in the binding energies (0.28 and 0.22 eV for W 4f and 0.31 and 0.32 eV for S 3d) were also observed for both W and Se after O_2 plasma treatment (shown as dashed lines). These results clearly proved that the oxygen radicals were effectively doped into the WSe_2 crystals during plasma exposure.

Next, we investigated the photoresponse of the pn-WSe_2 homojunction by measuring the I–V characteristics with monochromatic light illumination of different wavelengths, which displayed ideal diode characteristics as shown in Figure 4. Figure 4a,b illustrates the photoresponse studies of pn-WSe_2 at V_g = −60 V and +60 V, respectively. In addition, a clear photovoltaic effect at V_g = 0 V was observed for the pn-WSe_2 homojunction, signifying that the spontaneous charge separation took place with built-in potential at the junction, as shown in Figure 4c,d. Figure 4c illustrates the output characteristics of pn-WSe_2 measured in the dark and under 532 and 900 nm light illuminations. Under light illumination, the pn-WSe_2 homojunction exhibited short-circuit current values (I_{SC}, photocurrent at zero external bias) of 2.86 nA (for 532 nm) and 1.44 nA (900 nm) and open-circuit voltage values (V_{OC}, voltage with no current flowing) of 256 mV (532 nm) and 237 mV (900 nm). Hence, the pn-WSe_2 homojunctions are suggested for the applications of photovoltaic cells. In addition, Figure 4d shows the photovoltaic characteristics of the pn-WSe_2 homojunction illuminated with different wavelengths ranging from 400 to 900 nm.

We explored the optoelectronic properties of three different types of WSe_2 photodetectors, i.e., n-WSe_2 (as-fabricated), p-WSe_2 (O_2 plasma-doped), and pn-WSe_2 homojunction FETs, as illustrated in Figure 5 by carrying out electrical measurements in an ambient environment in the dark and laser illuminations. Here, we employed two lasers with wavelengths (λ_{Laser}) of 520 nm (visible) and 852 nm (near-IR) for the illuminations, and the schematic of laser illuminations are depicted in Figure 5a,b, respectively. Initially, the photocurrent generated from the as-fabricated WSe_2 photodetector was analyzed by illuminating λ_{Laser} = 520 nm with various powers, as shown in Figure S4 (Supporting Information). As the power of the laser increased, the photocurrent generated increased monotonically with increasing power and a medium-ranged power of 0.31 mW was considered for further investigations of photocurrent analysis to avoid the device heating with high laser power. Correspondingly, we considered the power of 0.075 mW for λ_{Laser} = 852 nm. The typical transfer curves of three types of WSe_2 photodetectors are displayed in Figure 5c−e. Figure 5c shows the transfer curves of as-fabricated WSe_2 (n-WSe_2) measured in darkness and under λ_{Laser} = 520 nm (power of 0.31 mW) and λ_{Laser} = 852 nm (power of 0.075

https://dx.doi.org/10.1021/acsami.9b23450
ACS Appl. Mater. Interfaces 2020, 12, 23261−23271

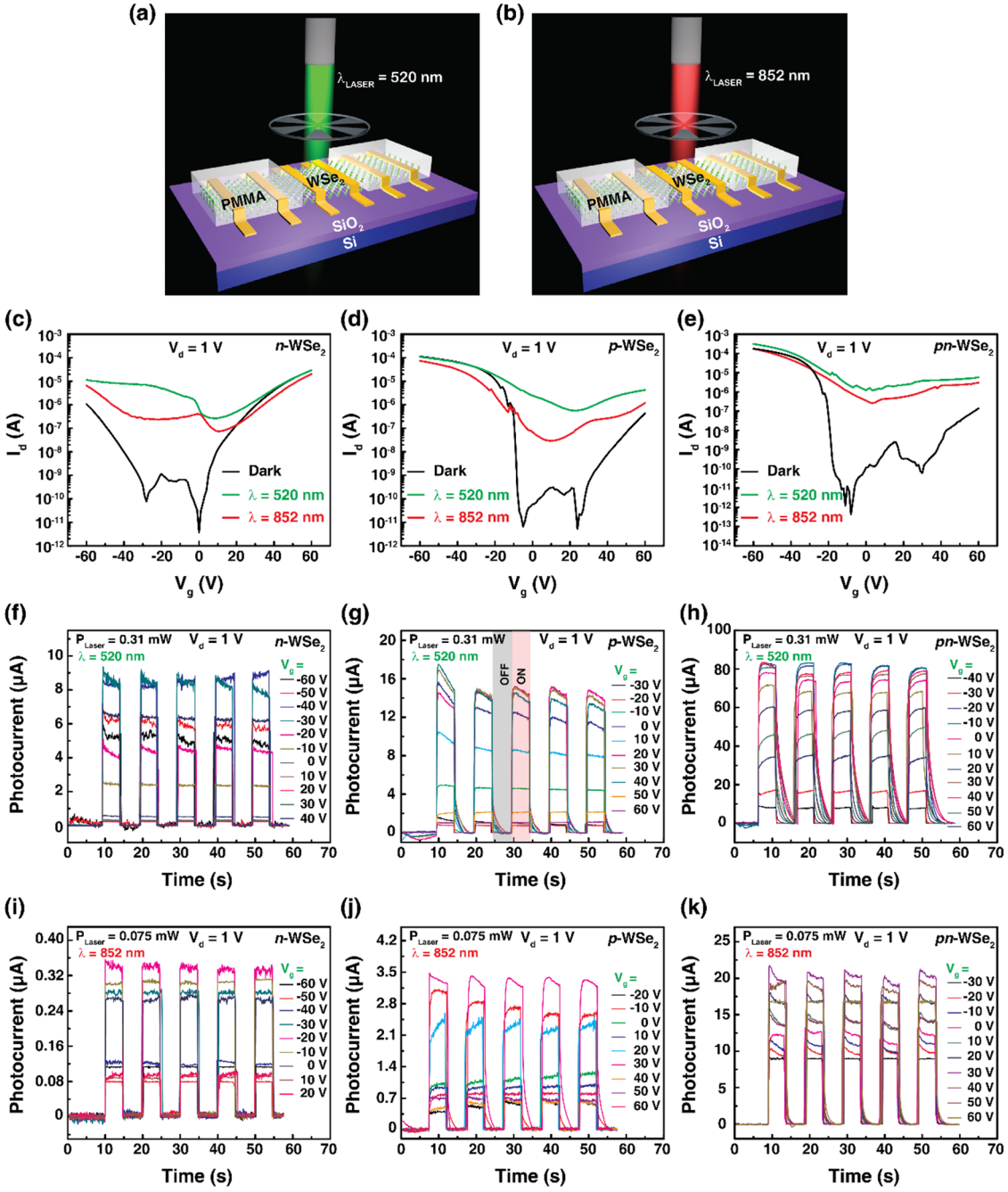

Figure 5. Optoelectronic characteristics of as-fabricated and O_2 plasma-doped WSe_2 FET devices. (a, b) Cartoon demonstration of the WSe_2 photodetector under 520 and 852 nm laser illuminations, respectively. Typical transfer characteristics of (c) n-WSe_2 (before O_2 plasma treatment), (d) p-WSe_2, and (e) pn-WSe_2 after O_2 plasma treatment measured in darkness and under laser illuminations of visible (520 nm) and near-infrared (852 nm) wavelengths. (f–h) Time-dependent photocurrent measurements of n-WSe_2, p-WSe_2, and pn-WSe_2 achieved under λ_{Laser} = 520 nm (P_{Laser} = 0.31 mW) at applied V_d = 1 V with various V_g's. (i–k) Time-dependent photocurrent measurements of n-WSe_2, p-WSe_2, and pn-WSe_2 achieved under λ_{Laser} = 852 nm (P_{Laser} = 0.075 mW) at applied V_d = 1 V with various V_g's.

mW) laser illuminations at applied drain bias (V_d = 1 V). As V_g varied, prominent and small variations in photocurrent (I_{photo}) were observed at V_g < 0 V and V_g > 0 V, respectively, which indicated that the photocurrent was effectively controlled by the applied gate bias. It was clearly witnessed that the off-state current values measured in the dark exhibited the significant enhancement in the I_{photo} from 3.66×10^{-12} A (I_{dark}) to 6.62×10^{-7} A (for λ_{Laser} = 520 nm) and 3.97×10^{-7} A (for λ_{Laser} = 852 nm) after laser illuminations at V_g = 0 V. From Figure 5d,e, the transfer curves of p- and pn-WSe_2 displayed I_{photo} enhancement at V_g = −5 and −8 V, respectively. The minimum I_{dark} observed at V_g = −5 V in p-WSe_2 exhibited substantial increment in I_{photo} from 6.62×10^{-12} to 4.1×10^{-6} A for λ_{Laser} = 520 nm and 1.5×10^{-7} A for λ_{Laser} = 852 nm. Similarly, the I_{dark} observed at V_g = −8 V in pn-WSe_2 showed significant increment in I_{photo} from 4.35×10^{-13} to 1.08×10^{-6} A and 2.29×10^{-7} A for λ_{Laser} = 520 and 852 nm, respectively. This enhancement was mainly ascribed to the strong light absorption in WSe_2 photodetectors generating a greater number of photoinduced electron–hole pairs and significant

https://dx.doi.org/10.1021/acsami.9b23450
ACS Appl. Mater. Interfaces 2020, 12, 23261−23271

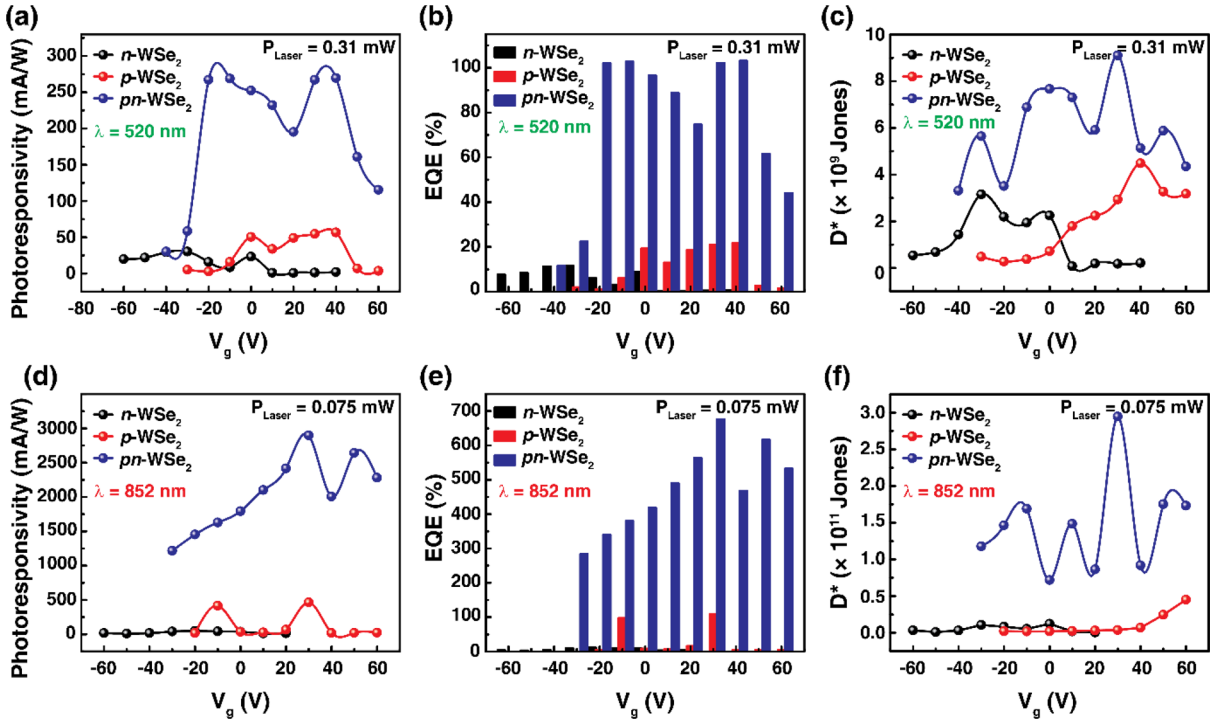

Figure 6. Photocurrent analysis of WSe_2 photodetectors. (a–c) Photoresponsivity (R), EQE (%), and detectivity (D^*) of n-WSe_2, p-WSe_2, and pn-WSe_2 obtained under λ_{Laser} = 520 nm as a function of V_g. (d–f) R, EQE (%), and D^* of n-WSe_2, p-WSe_2, and pn-WSe_2 obtained under λ_{Laser} = 852 nm as a function of V_g.

reduction in the Schottky barrier that allowed the photogenerated carriers to transmit more effectively along the WSe_2/metal interface with externally applied bias.[17,36] To further investigate the performance of WSe_2 photodetectors and to study their photoresponse dynamics, we performed the time- and gate voltage-dependent photocurrent measurements at fixed drain bias (V_d = +1 V), as demonstrated in Figure 5f–h and Figure 5i–k for 520 nm (power of 0.31 mW) and 852 nm (0.075 mW) laser illuminations, respectively. From the time-dependent photocurrent measurements of n-WSe_2 shown in Figure 5f for λ_{Laser} = 520 nm, as the V_g swept from −60 to +40 V, the photocurrent enhancement was clearly observed, reached the maximum photocurrent at V_g = −30 V, and decreased with a further increase in V_g. For p-WSe_2 and pn-WSe_2, the V_g was swept from −30 to +60 V and −40 to +60 V and exhibited the maximum photocurrent at V_g = +20 and −10 V, as illustrated in Figure 5g,h, respectively. Similarly, for the time-dependent photocurrent measurements under λ_{Laser} = 852 nm illuminations for n-WSe_2, p-WSe_2, and pn-WSe_2, the V_g sweep was applied from −60 to +20 V, −20 to +60 V, and −30 to +60 V, and high photoresponses were observed at V_g = −20, +30, and + 30 V, respectively, as shown in Figure 5i–k. Interestingly, this similar trend was also witnessed from the transfer curves with different applied V_g values (Figure 5c–e). The area-weighted photocurrents were compared since the areas of n-WSe_2 ($L \times W$: 4 μm × 16 μm), p-WSe_2 ($L \times W$: 3 μm × 16 μm), and pn-WSe_2 ($L \times W$: 8 μm × 16 μm) channels are not similar. From Figure 5f–h, the photocurrents observed at V_g = 0 V for n-WSe_2, p-WSe_2, and pn-WSe_2 with λ_{Laser} = 520 nm illuminations were 6.35, 13, and 77.9 μA, and the area-weighted photocurrents were 0.1, 0.27, and 0.61 $\mu A/\mu m^2$, respectively, resulting in 6-fold and 2.2-fold increments for pn-WSe_2 compared to n-WSe_2 and p-WSe_2. Similarly, for λ_{Laser} = 852 nm, the photocurrent values observed for n-WSe_2, p-WSe_2, and pn-WSe_2 at V_g = 0 V were 0.27, 1.15, and 13 μA, and the area-weighted photocurrents were 4.3, 24.5, and 101 $nA/\mu m^2$, respectively, resulting in 23.5-fold and 4-fold increments for pn-WSe_2 compared to n-WSe_2 and p-WSe_2. This significant photocurrent enhancement in pn-WSe_2 homojunctions after the surface modification was attributed to the generation of excess electron–hole pairs with strong light absorption in the junction and reduction of the probability of recombination of the photoactivated charge carriers. This substantial photocurrent generation at various V_g and positive V_d conditions resulted from the pn-WSe_2 homojunction perhaps used as a phototransistor for light detection from visible to near-IR spectra.

We compared the photodetector performances among n-WSe_2, p-WSe_2, and pn-WSe_2 devices by evaluating the photoresponse figures of merit such as photoresponsivity (R), external quantum efficiency (EQE), detectivity (D^*), and rise (t_r) and fall times (t_f), as demonstrated in Figure 6 and Figure S5 (Supporting Information). The spectral responses of WSe_2 photodetectors were expressed through R, which is defined as the ratio of the photocurrent and incident laser power, i.e., $R = I_{photo}/P_{Laser}$, where $I_{photo} = I_{dark} - I_{light}$. Figure 6a,d illustrates the photoresponsivities of WSe_2 photodetectors as a function of V_g for 520 and 852 nm laser illumination wavelengths, respectively obtained from the time- and voltage-dependent curves. It was clearly observed that the R of the pn-WSe_2 homojunction photodetector was higher compared to those of n-WSe_2 and p-WSe_2 devices. Owing to the formation of the depletion region in the junction devices, the photon collection efficiency was improved and, hence, the responsivity increased. Another crucial figure of merit of photodetector is EQE, which is stated as the total number of charge carriers generated for the number of incident photons on photodetectors and given by EQE (%) = $(hcR/e\lambda) \times 100$, where h, c,

https://dx.doi.org/10.1021/acsami.9b23450
ACS Appl. Mater. Interfaces 2020, 12, 23261–23271

Table 1. Performance Comparisons of O_2 Plasma-Treated WSe_2 FET Photodetectors with Reported Intrinsic or Doped Two-Dimensional Material Photodetectors

device (method)	operation conditions (wavelength, bias)	responsivity (mA/W)	EQE (%)	detectivity (Jones)	response time (ms)	reference
WSe_2 (intrinsic)	532 nm (V_d = 2 V; V_g = −12 V)	7000	40		0.04	15
WSe_2 (intrinsic)	635 nm (V_d = 0.2 V)	900	180		900	37
MoS_2 (intrinsic)	550 nm (V_d = 0 V; V_g = 1 V)	0.42				38
WSe_2 (chemical doping)	650 nm (V_d = 1 V; V_g = −60 V)	360		1×10^9	310	39
WSe_2 (chemical doping)	532 nm (V_d = −0.5 V; V_g = 0 V)	20	13			40
WSe_2/MoS_2 (heterojunction)	500 nm (V_d = −3 V)	170			0.1	41
WSe_2/MoS_2 (heterojunction)	660 nm (V_d = 2 V; V_g = 10 V)	17,800			80	42
WSe_2 (chemical doping)	635 nm (V_d = 5 V; V_g = −40 V)	468	91.2		4	43
MoS_2 (chemical doping)	500 nm (V_d = −1.5 V; V_g = 0 V)	330	81	1.6×10^{10}	100−200	5
n-WSe_2	520 nm (V_d = 1 V; V_g = 0 V)	20	8.7	2.5×10^9	50.2	this work
	852 nm (V_d = 1 V; V_g = 0 V)	23	11	2.3×10^{10}	68.3	
p-WSe_2 (O_2 plasma doping)	520 nm (V_d = 1 V; V_g = 0 V)	7	2.4	9×10^8	46.5	this work
	852 nm (V_d = 1 V; V_g = 0 V)	37.7	15	1×10^{10}	61.2	
pn-WSe_2 homojunction (O_2 plasma doping)	520 nm (V_d = 1 V; V_g = 0 V)	250	97	7.7×10^9	41.8	this work
	852 nm (V_d = 1 V; V_g = 0 V)	2000	420	7.2×10^{10}	53.7	

e, and λ are Planck's constant (6.63×10^{-34} J·s), the velocity of light (3×10^8 m·s^{-1}), the electron charge (1.6×10^{-19} C), and the laser illumination wavelength (λ_{Laser} = 520 and 852 nm), respectively. We compared the EQE for pn-WSe_2 homojunction photodetectors with n-WSe_2 and p-WSe_2 devices for 520 and 852 nm laser illumination wavelengths, as shown in Figure 6b,e, and clearly showed that the homojunction photodetectors resulted in higher EQE at all the applied V_g's. The EQE values for the pn-WSe_2 photodetector at V_g = 0 V were 97% for 520 nm wavelength and 420% for 852 nm wavelength, which were higher than previously reported.[7,15,16] Further, the photogain (G) is extracted to quantify the photosensitivity of the junction, which is proportional to R, defined by the equation $R = (EQE \cdot G \cdot e)/(h\upsilon)$, where υ is the frequency of the laser. From the above relation, if the EQE is assumed as 1, then the G values estimated for n-WSe_2, p-WSe_2, and pn-WSe_2 are 1, 3, and 10 for 520 nm and 1, 5, and 49 for 852 nm, respectively, at V_g = 0 V.

In addition, D^* is another figure of merit for photodetector devices that designates the magnitude of detector sensitivity, given by D^* (Jones) = $(R \cdot A^{1/2})/(2e \cdot I_{dark})^{1/2}$, where $A = W \times L$ is the area of the device (W is the width and L is the length of the channel). The areas of n-WSe_2, p-WSe_2, and pn-WSe_2 were 4 μm × 16 μm, 3 μm × 16 μm, and 8 μm × 16 μm, respectively. The comparisons of D^* for WSe_2 photodetectors are displayed in Figure 6c,f. The obtained D^* values for the homojunction photodetector at V_g = 0 were 5.9×10^9 Jones at 520 nm wavelength and 2.95×10^{11} Jones at 852 nm wavelength. In addition, we evaluated the rise time (t_r) and fall time (t_f) to determine the speed of the device by plotting a single ON/OFF photocurrent cycle (V_d = 1 V; V_g = 0 V) and compared them as shown in Figure S5 (Supporting Information). The times taken to increase the saturation photocurrent from 10 to 90% and decrease it from 90 to 10% are designated as t_r and t_f, respectively. The t_r and t_f obtained under λ_{Laser} = 520 nm were 50 and 70 ms for the n-WSe_2 photodetector, 45.6 and 302.9 ms for the p-WSe_2 photodetector, and 41.8 and 2289.8 ms for the pn-WSe_2 photodetector. Likewise, the t_r and t_f obtained for n-, p-, and pn-WSe_2 photodetectors under λ_{Laser} = 852 nm were 59.3 and 89.3 ms, 57 and 100.84 ms, and 53.7 ms and 1027.5 ms, respectively. Here, the t_r indicated the speed of the photodetector device, and therefore, we considered that the improvement in t_r (smaller for pn-WSe_2) resulted in a faster response of the device, compared to n- and p-WSe_2, and also ascribed to a higher carrier density in the junction devices. Besides, the higher t_f (slow decay) indicated the oxygen photochemical absorption and desorption of carriers on WO_x (observed in *pn*-WSe_2) and also ascribed to the excess lifetime of trapped carriers even after the termination of light illumination. We also expected that due to the higher photocurrent (in pn-WSe_2), a lot of photocarriers generated need more time to relax. Hence, the t_r's of pn-WSe_2 photodetectors were faster than those of *n*- and *p*-WSe_2, while the t_f's were relatively slower.

Furthermore, we investigated the thickness-dependent WSe_2 photodetector performances with different thicknesses such as 6 nm (~8 layers) and 1.8 nm (bilayer) to compare the responsivities under various monochromator wavelengths. Figures S6−S8 (Supporting Information) illustrate the complete optoelectronic characteristics and photoresponsivity analysis of thick and thin WSe_2 FET devices before and after O_2 plasma treatment. It was noticed that the O_2 plasma treatment converts the bilayer WSe_2 (band gap of ~1.4 eV) into monolayer WSe_2 (1.6 eV), similarly observed from a previous report.[33] Hence, it was anticipated from the studies that the O_2 plasma-treated bilayer WSe_2 FET photodetectors were inadequate for sensing in the IR region. Therefore, our results depict that the bulk WSe_2 can be used for broadband photodetector applications, which ranged from visible (400 nm) to near-IR (900 nm) regions. Additionally, we have determined the optoelectrical characteristics of as-fabricated WSe_2 channels covered with and without PMMA to observe the dielectric screening effect, as shown in Figure S2 (Supporting Information). From the results, it was shown that PMMA does not influence the electrical properties; rather, similar results were seen in photodetection for both channels without and with PMMA under 532 and 700 nm illuminations. To compare the performance of our fabricated WSe_2 pn-homojunction photodetector to the literature, we have summarized the figures of merit in Table 1.

To further confirm that the enhanced photocurrent generation was actually from the junction created from p-WSe_2 and n-WSe_2, we used scanning photocurrent microscopy

https://dx.doi.org/10.1021/acsami.9b23450
ACS Appl. Mater. Interfaces 2020, 12, 23261−23271

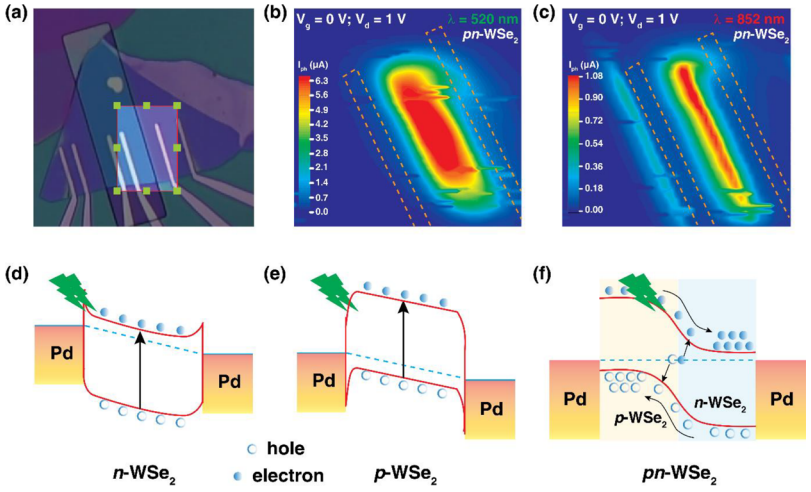

Figure 7. Photocurrent mapping studies. (a) OM image of the O_2 plasma-treated WSe_2 FET photodetector used for photocurrent mapping. The area to be measured is represented in a rectangular box. (b, c) Scanning photocurrent mapping results of the pn-WSe_2 FET photodetector taken at V_g = 0 V and V_d = 1 V under λ_{Laser} = 520 and 852 nm illuminations, respectively. (d–f) Energy band diagrams of n-WSe_2, p-WSe_2, and pn-WSe_2 represented under light illuminations.

(SPCM) to map the photocurrent. Figure 7a displays an OM of the pn-WSe_2 device with a rectangular portion designating the scanned area. The photocurrent mapping images of the pn-WSe_2 photodetector illuminated under λ_{Laser} = 520 and 852 nm at V_d = 1 V and V_g = 0 V are demonstrated in Figure 7b,c, respectively. The electrodes were represented with dashed lines to distinguish the photocurrent generated in the channel. It was clearly observed that the photocurrent generated mostly from the pn-junction region of WSe_2 at zero gate bias. A video captured during the photocurrent mapping measurement for pn-WSe_2 under 852 nm laser illumination is shown in Video S1 (Supporting Information). The photocurrent characteristics of the junction can be further understood through the energy band diagrams, as shown in Figure 7d–f. When the energy of illuminated light is greater than the band gap of the material, the electrons are excited from the valence band to the conduction band, and the photon absorptions produce more electron–hole pairs, which were then separated by a built-in electric field and external drain bias (V_d), and reduces the recombination of electron–hole pairs to generate a high photocurrent. When the channel is modified with O_2 plasma to achieve a junction and as the laser is illuminated, the generation of electron–hole pairs takes place near the depletion region and the photoexcited carriers are swept from the junction in opposite directions by externally applied bias, resulting in a net increase in photocurrent.

MATERIALS AND METHODS

Fabrication of n-Type and O_2 Plasma-Treated (p-Type) WSe_2 FETs. The WSe_2 crystals were obtained from HQ Graphene, the Netherlands. Prior to device fabrication, the heavily doped p-type Si substrates coated with a thermally oxidized SiO_2 layer (with a thickness of 285 nm, which was used as a backgate oxide layer) were cleaned thoroughly in acetone, isopropyl alcohol (IPA), and ethanol using ultrasonication for 15 min followed by drying with N_2 blow. The few-layer-thick WSe_2 were mechanically exfoliated using Scotch tape on the p-type Si/SiO_2 substrate. The WSe_2 flakes were scanned and chosen selectively by an optical microscope. The source and drain electrodes were patterned by electron beam lithography (EBL), and the metal electrode Pd (50 nm) was deposited using electron beam deposition. Later, the p-type WSe_2 devices were achieved by treating the as-fabricated WSe_2 channel with O_2 plasma (p-type dopant). The plasma treatment was performed by an O_2 plasma source under the following operating conditions: 13.56 MHz RF, 50 W power, 8.0 × 10^{-6} Torr base pressure, 30 mTorr working pressure, 30 SCCM O_2 flow rate, and 200 s plasma generation time.

Fabrication of WSe_2 Lateral pn-Homojunctions. Subsequently, we developed the WSe_2 lateral pn-homojunctions from the as-fabricated WSe_2 FETs as follows. The as-fabricated WSe_2 devices (as shown in Figure 1b) were spin-coated with PMMA A4 495 (Microchem) at a speed of 4000 rpm for 60 s followed by annealing on a hot plate at 180 °C for 90 s. Consecutively, PMMA A6 950 (Microchem) was also spin-coated on top of PMMA A4 with the same procedure as above. To achieve pn-homojunctions, we opened a portion of a channel near the electrode using EBL followed by development with a developer (a mixture of isopropyl alcohol (IPA) and deionized water in a 3:1 ratio) for a few seconds, rinsed with IPA, and then dried using N_2 gas blowing. Subsequently, the opened channels were doped with O_2 plasma (procedure as in above section) to achieve lateral pn-homojunctions from WSe_2 (as shown in Figure 2b).

Device Characterization. *Atomic Force Microscopy (AFM).* AFM was performed by placing the sample on a metal puck, which was connected to the ground. All the AFM images were taken at room temperature under atmospheric pressure and dehumidification condition (<25%) under noncontact mode.

Optical, Raman, and Photoluminescence (PL) Measurements. All the optical images of the devices were acquired from an Olympus BX51 microscope with an attached video camera. The Raman and PL measurements were conducted with a micro-Raman spectroscopy system equipped with 532 nm laser wavelength (spot size, ~2 μm) operated at 0.2 mW laser power and a Xe-arc lamp-equipped fluorometer with a power of 0.2 mW, respectively.

X-ray Photoelectron Spectroscopy (XPS) Measurement. XPS analysis was executed for as-fabricated WSe_2 and O_2 plasma-treated WSe_2 samples fabricated on Si/SiO_2 substrates with an ESCALAB 250Xi spectrometer (Thermo Scientific, UK). A monochromatic Al Kα (1486.6 eV) X-ray source was used to irradiate the device with a 600 μm-diameter spot size. The complete survey and the high-resolution deconvoluted spectra were measured for as-fabricated and O_2 plasma-treated WSe_2 devices.

Electrical (I–V) and Photocurrent Measurements. All the electrical and photocurrent measurements were performed using a semiconductor parameter analyzer (Keithley 4200) in ambient conditions at room temperature. For the measurements of photo-response characteristics, solid-state laser diodes with different wavelengths, i.e., 520 and 852 nm, were used as an illumination

https://dx.doi.org/10.1021/acsami.9b23450
ACS Appl. Mater. Interfaces 2020, 12, 23261–23271

source. The incident power of the lasers was measured with an optical power meter (Newport model 1918-C) and thermopile sensor (919P-003-10). The detailed experimental setup is illustrated in Figure S1 (Supporting Information). We also measured the photoresponse characteristics with a monochromator light source producing different wavelengths ranging from 400 to 900 nm. The power value varies on the power level of mW and μW for laser and monochromator light source illuminations, respectively.

CONCLUSIONS

We developed lateral pn-homojunctions formed from bulk WSe_2 via oxygen plasma doping, and these pn-homojunctions demonstrated gate-modulated broadband photodetector applications. The polarity change from n-type to p-type was clearly observed from transfer curves after O_2 plasma doping, and this enabled us to develop a WSe_2 lateral pn-homojunction. The WSe_2 lateral pn-homojunctions exhibited an increase in photoresponse for various wavelengths, which resulted in V_{OC} and I_{SC} originating from the pn-junction formed after O_2 plasma treatment. We executed the gate-dependent photoresponse properties of WSe_2 photodetector FETs before and after O_2 plasma treatment upon visible (520 nm) and near-infrared laser (852 nm) illuminations, which led to the significant enhancement in photoresponse for the homojunction devices at V_g = 0 V and V_d = +1 V. The devices exhibited excellent photoresponsivity, EQE (%), and detectivity with a short response time at room temperature. We confirmed by scanning photocurrent microscopy that the prominent photoresponse originated from the junctions. Hence, this work furnishes an industry-compatible plasma doping technique to fabricate pn-homojunctions to improve the optoelectronic properties of 2D materials.

ASSOCIATED CONTENT

Supporting Information

The Supporting Information is available free of charge at https://pubs.acs.org/doi/10.1021/acsami.9b23450.

Schematic diagram of the SPCM measurement setup, photocurrent comparisons of WSe_2 without and with PMMA, time-dependent photocurrent measurements of n-WSe_2 measured under λ_{Laser} = 520 nm with various laser powers (mW), response time comparisons, and optoelectronic characteristics and photoresponsivity comparisons of as-fabricated and O_2 plasma-doped thick and thin WSe_2 FET devices (PDF)

Scanning photocurrent mapping video of pn-WSe_2 under 852 nm laser illumination displaying the photocurrent generation in the junction part (MP4)

AUTHOR INFORMATION

Corresponding Author

Won Jong Yoo − *SKKU Advanced Institute of Nano Technology (SAINT), Sungkyunkwan University, Suwon, Gyeonggi-do 16419, Republic of Korea;* orcid.org/0000-0002-3767-7969; Email: yoowj@skku.edu

Authors

Sekhar Babu Mitta − *SKKU Advanced Institute of Nano Technology (SAINT), Sungkyunkwan University, Suwon, Gyeonggi-do 16419, Republic of Korea;* orcid.org/0000-0002-8011-5291

Fida Ali − *SKKU Advanced Institute of Nano Technology (SAINT), Sungkyunkwan University, Suwon, Gyeonggi-do 16419, Republic of Korea*

Zheng Yang − *SKKU Advanced Institute of Nano Technology (SAINT), Sungkyunkwan University, Suwon, Gyeonggi-do 16419, Republic of Korea*

Inyong Moon − *SKKU Advanced Institute of Nano Technology (SAINT), Sungkyunkwan University, Suwon, Gyeonggi-do 16419, Republic of Korea*

Faisal Ahmed − *Department of Mechanical Engineering, College of Electrical and Mechanical Engineering, National University of Science and Technology, Islamabad 44000, Pakistan*

Tae Jin Yoo − *School of Materials Science and Engineering, Center for Emerging Electronic Devices and Systems, Gwangju Institute of Science and Technology, Gwangju 61005, Republic of Korea*

Byoung Hun Lee − *School of Materials Science and Engineering, Center for Emerging Electronic Devices and Systems, Gwangju Institute of Science and Technology, Gwangju 61005, Republic of Korea;* orcid.org/0000-0002-4540-7731

Complete contact information is available at: https://pubs.acs.org/10.1021/acsami.9b23450

Notes

The authors declare no competing financial interest.

ACKNOWLEDGMENTS

This work was supported by the Global Research Laboratory (GRL) Program (2016K1A1A2912707) and Global Frontier R&D Program (2013M3A6B1078873), both funded by the National Research Foundation of Korea (NRF).

REFERENCES

(1) Wang, Q. H.; Kalantar-Zadeh, K.; Kis, A.; Coleman, J. N.; Strano, M. S. Electronics and Optoelectronics of Two-Dimensional Transition Metal Dichalcogenides. *Nat. Nanotechnol.* **2012**, *7*, 699−712.

(2) Zhang, W.; Chiu, M. H.; Chen, C. H.; Chen, W.; Li, L. J.; Wee, A. T. S. Role of Metal Contacts in High-Performance Phototransistors Based on WSe_2 Monolayers. *ACS Nano* **2014**, *8*, 8653−8661.

(3) Luo, X.; Andrews, K.; Wang, T.; Bowman, A.; Zhou, Z.; Xu, Y. Q. Reversible Photo-Induced Doping in WSe_2 Field Effect Transistors. *Nanoscale* **2019**, *11*, 7358−7363.

(4) Ross, J. S.; Klement, P.; Jones, A. M.; Ghimire, N. J.; Yan, J.; Mandrus, D. G.; Taniguchi, T.; Watanabe, K.; Kitamura, K.; Yao, W.; Cobden, D. H.; Xu, X. Electrically Tunable Excitonic Light-Emitting Diodes Based on Monolayer WSe_2 p-n Junctions. *Nat. Nanotechnol.* **2014**, *9*, 268−272.

(5) Choi, M. S.; Qu, D.; Lee, D.; Liu, X.; Watanabe, K.; Taniguchi, T.; Yoo, W. J. Lateral MoS_2 p−n Junction Formed by Chemical Doping for Use in High-Performance Optoelectronics. *ACS Nano* **2014**, *8*, 9332−9340.

(6) Li, H. M.; Lee, D.; Qu, D.; Liu, X.; Ryu, J.; Seabaugh, A.; Yoo, W. J. Ultimate Thin Vertical p-n Junction Composed of Two-Dimensional Layered Molybdenum Disulfide. *Nat. Commun.* **2015**, *6*, 6564.

(7) Cheng, R.; Li, D.; Zhou, H.; Wang, C.; Yin, A.; Jiang, S.; Liu, Y.; Chen, Y.; Huang, Y.; Duan, X. Electroluminescence and Photocurrent Generation from Atomically Sharp WSe_2/MoS_2 Heterojunction p-n Diodes. *Nano Lett.* **2014**, *14*, 5590−5597.

(8) Lee, C. H.; Lee, G. H.; Van Der Zande, A. M.; Chen, W.; Li, Y.; Han, M.; Cui, X.; Arefe, G.; Nuckolls, C.; Heinz, T. F.; Guo, J.; Hone, J.; Kim, P. Atomically Thin p-n Junctions with van Der Waals Heterointerfaces. *Nat. Nanotechnol.* **2014**, *9*, 676−681.

(9) Deng, Y.; Luo, Z.; Conrad, N. J.; Liu, H.; Gong, Y.; Najmaei, S.; Ajayan, P. M.; Lou, J.; Xu, X.; Ye, P. D. Black Phosphorus-Monolayer MoS_2 van Der Waals Heterojunction p-n Diode. *ACS Nano* **2014**, *8*, 8292−8299.
(10) Groenendijk, D. J.; Buscema, M.; Steele, G. A.; Michaelis De Vasconcellos, S.; Bratschitsch, R.; Van Der Zant, H. S. J.; Castellanos-Gomez, A. Photovoltaic and Photothermoelectric Effect in a Double-Gated WSe_2 Device. *Nano Lett.* **2014**, *14*, 5846−5852.
(11) Jariwala, D.; Howell, S. L.; Chen, K. S.; Kang, J.; Sangwan, V. K.; Filippone, S. A.; Turrisi, R.; Marks, T. J.; Lauhon, L. J.; Hersam, M. C. Hybrid, Gate-Tunable, van der Waals p−n Heterojunctions from Pentacene and MoS_2. *Nano Lett.* **2016**, *16*, 497−503.
(12) Das, S.; Appenzeller, J. WSe_2 Field Effect Transistors with Enhanced Ambipolar Characteristics. *Appl. Phys. Lett.* **2013**, *103*, 103501.
(13) Tosun, M.; Chuang, S.; Fang, H.; Sachid, A. B.; Hettick, M.; Lin, Y.; Zeng, Y.; Javey, A. High-Gain Inverters Based on WSe_2 Complementary Field-Effect Transistors. *ACS Nano* **2014**, *8*, 4948−4953.
(14) Chuang, H. J.; Tan, X.; Ghimire, N. J.; Perera, M. M.; Chamlagain, B.; Cheng, M. M. C.; Yan, J.; Mandrus, D.; Tománek, D.; Zhou, Z. High Mobility WSe_2 p- and n- Type Field-Effect Transistors Contacted by Highly Doped Graphene for Low-Resistance Contacts. *Nano Lett.* **2014**, *14*, 3594−3601.
(15) Pradhan, N. R.; Ludwig, J.; Lu, Z.; Rhodes, D.; Bishop, M. M.; Thirunavukkuarasu, K.; McGill, S. A.; Smirnov, D.; Balicas, L. High Photoresponsivity and Short Photoresponse Times in Few-Layered WSe_2 Transistors. *ACS Appl. Mater. Interfaces* **2015**, *7*, 12080−12088.
(16) Baugher, B. W. H.; Churchill, H. O. H.; Yang, Y.; Jarillo-Herrero, P. Optoelectronic Devices Based on Electrically Tunable p-n Diodes in a Monolayer Dichalcogenide. *Nat. Nanotechnol.* **2014**, *9*, 262−267.
(17) Xie, Y.; Wu, E.; Hu, R.; Qian, S.; Feng, Z.; Chen, X.; Zhang, H.; Xu, L.; Hu, X.; Liu, J.; Zhang, D. Enhancing Electronic and Optoelectronic Performances of Tungsten Diselenide by Plasma Treatment. *Nanoscale* **2018**, *10*, 12436−12444.
(18) Lee, D. S.; Kim, J. Y.; Shin, D. Y.; Lee, Y.; Kim, J.; Lee, S. J.; Joo, J. Significantly Increased Photoresponsivity of WSe_2-Based Transistors through Hybridization with Gold-Tetraphenylporphyrin as Efficient n-Type Dopant. *Adv. Electron. Mater.* **2019**, *5*, 1800802.
(19) Addou, R.; Smyth, C. M.; Noh, J.-Y.; Lin, Y.-C.; Pan, Y.; Eichfeld, S. M.; Fölsch, S.; Robinson, J. A.; Cho, K.; Feenstra, R. M.; Wallace, R. M. One Dimensional Metallic Edges in Atomically Thin WSe_2 Induced by Air Exposure. *2D Mater.* **2018**, *5*, No. 025017.
(20) Yamamoto, M.; Dutta, S.; Aikawa, S.; Nakaharai, S.; Wakabayashi, K.; Fuhrer, M. S.; Ueno, K.; Tsukagoshi, K. Self-Limiting Layer-by-Layer Oxidation of Atomically Thin WSe_2. *Nano Lett.* **2015**, *15*, 2067−2073.
(21) Wang, S.; Zhao, W.; Giustiniano, F.; Eda, G. Effect of Oxygen and Ozone on p-Type Doping of Ultra-Thin WSe_2 and $MoSe_2$ Field Effect Transistors. *Phys. Chem. Chem. Phys.* **2016**, *18*, 4304−4309.
(22) Yamamoto, M.; Nakaharai, S.; Ueno, K.; Tsukagoshi, K. Self-Limiting Oxides on WSe_2 as Controlled Surface Acceptors and Low-Resistance Hole Contacts. *Nano Lett.* **2016**, *16*, 2720−2727.
(23) Moon, I.; Lee, S.; Lee, M.; Kim, C.; Seol, D.; Kim, Y.; Kim, K. H.; Yeom, G. Y.; Teherani, J. T.; Hone, J.; Yoo, W. J. The Device Level Modulation of Carrier Transport in a 2D WSe_2 Field Effect Transistor via a Plasma Treatment. *Nanoscale* **2019**, *11*, 17368−17375.
(24) Fang, H.; Chuang, S.; Chang, T. C.; Takei, K.; Takahashi, T.; Javey, A. High-Performance Single Layered WSe_2 p-FETs with Chemically Doped Contacts. *Nano Lett.* **2012**, *12*, 3788−3792.
(25) Zhao, P.; Kiriya, D.; Azcatl, A.; Zhang, C.; Tosun, M.; Liu, Y. S.; Hettick, M.; Kang, J. S.; McDonnell, S.; Kc, S.; Guo, J.; Cho, K.; Wallace, R. M.; Javey, A. Air Stable p-Doping of WSe_2 by Covalent Functionalization. *ACS Nano* **2014**, *8*, 10808−10814.
(26) Koppens, F. H. L.; Mueller, T.; Avouris, P.; Ferrari, A. C.; Vitiello, M. S.; Polini, M. Photodetectors Based on Graphene, Other Two-Dimensional Materials and Hybrid Systems. *Nat. Nanotechnol.* **2014**, *9*, 780−793.
(27) Long, M.; Liu, E.; Wang, P.; Gao, A.; Xia, H.; Luo, W.; Wang, B.; Zeng, J.; Fu, Y.; Xu, K.; et al. Broadband Photovoltaic Detectors Based on an Atomically Thin Heterostructure. *Nano Lett.* **2016**, *16*, 2254−2259.
(28) Liu, Y.; Shivananju, B. N.; Wang, Y.; Zhang, Y.; Yu, W.; Xiao, S.; Sun, T.; Ma, W.; Mu, H.; Lin, S.; Zhang, H.; Lu, Y.; Qiu, C.-W.; Li, S.; Bao, Q. Highly Efficient and Air-Stable Infrared Photodetector Based on 2D Layered Graphene−Black Phosphorus Heterostructure. *ACS Appl. Mater. Interfaces* **2017**, *9*, 36137−36145.
(29) Yu, W.; Li, S.; Zhang, Y.; Ma, W.; Sun, T.; Yuan, J.; Fu, K.; Bao, Q. Near-Infrared Photodetectors Based on $MoTe_2$/Graphene Heterostructure with High Responsivity and Flexibility. *Small* **2017**, *13*, 1−8.
(30) Deng, W.; Chen, Y.; You, C.; An, B.; Liu, B.; Li, S.; Zhang, Y.; Yan, H.; Sun, L. Visible-Infrared Dual-Mode MoS_2-Graphene-MoS_2 Phototransistor with High Ratio of the I_{ph}/I_{dark}. *2D Mater.* **2018**, *5*, No. 045027.
(31) Wei, X.; Yan, F.-G.; Shen, C.; Lv, Q.-S.; Wang, K.-Y. Photodetectors Based on Junctions of Two-Dimensional Transition Metal Dichalcogenides. *Chin. Phys. B* **2017**, *26*, No. 038504.
(32) Tosun, M.; Chan, L.; Amani, M.; Roy, T.; Ahn, G. H.; Taheri, P.; Carraro, C.; Ager, J. W.; Maboudian, R.; Javey, A. Air-Stable n-Doping of WSe_2 by Anion Vacancy Formation with Mild Plasma Treatment. *ACS Nano* **2016**, *10*, 6853−6860.
(33) Li, Z.; Yang, S.; Dhall, R.; Kosmowska, E.; Shi, H.; Chatzakis, I.; Cronin, S. B. Layer Control of WSe_2 via Selective Surface Layer Oxidation. *ACS Nano* **2016**, *10*, 6836−6842.
(34) Biloen, P.; Pott, G. T. X-Ray Photoelectron Spectroscopy Study of Supported Tungsten Oxide. *J. Catal.* **1973**, *30*, 169−174.
(35) Jaegermann, W.; Schmeisser, D. Reactivity of Layer Type Transition Metal Chalcogenides towards Oxidation. *Surf. Sci.* **1986**, *165*, 143−160.
(36) Jo, S. H.; Kang, D. H.; Shim, J.; Jeon, J.; Jeon, M. H.; Yoo, G.; Kim, J.; Lee, J.; Yeom, G. Y.; Lee, S.; Yu, H.-Y.; Choi, C.; Park, J.-H. A High-Performance WSe_2/h-BN Photodetector Using a Triphenylphosphine (PPh_3)-Based n-Doping Technique. *Adv. Mater.* **2016**, *28*, 4824−4831.
(37) Zheng, Z.; Zhang, T.; Yao, J.; Zhang, Y.; Xu, J.; Yang, G. Flexible, Transparent and Ultra-Broadband Photodetector Based on Large-Area WSe_2 Film for Wearable Devices. *Nanotechnology* **2016**, *27*, 225501.
(38) Yin, Z.; Li, H.; Li, H.; Jiang, L.; Shi, Y.; Sun, Y.; Lu, G.; Zhang, Q.; Chen, X.; Zhang, H. Single-Layer MoS_2 Phototransistors. *ACS Nano* **2012**, *6*, 74−80.
(39) Hu, C.; Dong, D.; Yang, X.; Qiao, K.; Yang, D.; Deng, H.; Yuan, S.; Khan, J.; Lan, Y.; Song, H.; Tang, J. Synergistic Effect of Hybrid PbS Quantum Dots/2D-WSe_2 Toward High Performance and Broadband Phototransistors. *Adv. Funct. Mater.* **2017**, *27*, 1603605.
(40) Ko, S.; Na, J.; Moon, Y. S.; Zschieschang, U.; Acharya, R.; Klauk, H.; Kim, G. T.; Burghard, M.; Kern, K. Few-Layer WSe_2 Schottky Junction-Based Photovoltaic Devices through Site-Selective Dual Doping. *ACS Appl. Mater. Interfaces* **2017**, *9*, 42912−42918.
(41) Lee, H. S.; Ahn, J.; Shim, W.; Im, S.; Hwang, D. K. 2D WSe_2/MoS_2van Der Waals Heterojunction Photodiode for Visible-near Infrared Broadband Detection. *Appl. Phys. Lett.* **2018**, *113*, 163102.
(42) Sun, M.; Fang, Q.; Xie, D.; Sun, Y.; Xu, J.; Teng, C.; Dai, R.; Yang, P.; Li, Z.; Li, W.; Zhang, Y. Novel Transfer Behaviors in 2D MoS_2/WSe_2 Heterotransistor and Its Applications in Visible-Near Infrared Photodetection. *Adv. Electron. Mater.* **2017**, *3*, 1600502.
(43) Yang, Y.; Huo, N.; Li, J. Gate-Tunable and High Optoelectronic Performance in Multilayer WSe_2p−n Diode. *J. Mater. Chem. C* **2018**, *6*, 11673−11678.

https://dx.doi.org/10.1021/acsami.9b23450
ACS Appl. Mater. Interfaces 2020, 12, 23261−23271